Defect Control Strategies for Al$_{1-x}$Gd$_x$N Alloys

Naseem Ud Din,[a] Cheng-Wei Lee,[a] Keisuke Yazawa,[b] William Nemeth,[b] Rebecca W. Smaha,[b] Nancy M. Haegel,[b] Prashun Gorai[a,b*]

Tetrahedrally-bonded III-N and related alloys are useful for a wide range of applications, from optoelectronics to dielectric electromechanics. Heterostructural AlN-based alloys offer unique properties for piezoelectrics, ferroelectrics, and other emerging applications. Atomic-scale point defects and impurities can strongly affect the functional properties of materials, and therefore, it is crucial to understand the nature of these defects and mechanisms through which their concentrations may be controlled in AlN-based alloys. In this study, we employ density functional theory with alloy modeling and point defect calculations to investigate native point defects and unintentional impurities in Al$_{1-x}$Gd$_x$N alloys. Among the native defects that introduce deep mid-gap states, nitrogen vacancies (V$_N$) are predicted to be in the highest concentration, especially under N-poor growth conditions. We predict and experimentally demonstrate that V$_N$ formation can be suppressed in thin films through growth in N-rich environments. We also find that Al$_{1-x}$Gd$_x$N alloys are prone to high levels of unintentional O incorporation, which indirectly leads to even higher concentrations of deep defects. Growth under N-rich/reducing conditions is predicted to minimize and partially alleviate the effects of O incorporation. The results of this study provide valuable insights into the defect behavior in wurtzite nitride-based alloys, which can guide their design and optimization for various applications

1 Introduction

Alloying of ultra-wide band gap aluminum nitride (AlN) with other III-nitrides has unlocked attractive optoelectronic and electromechanical properties that have been utilized for developing ultra-violet light-emitting diodes,[1] resonators[2,3] etc. For example, AlN is commonly alloyed with isostructural GaN and InN to tailor its optoelectronic properties for light-emitting diodes.[4] More recently, AlN has been alloyed with heterostructural ScN (rocksalt) and BN (hexagonal) to tune its piezo- and ferro-electric properties.[5–10] AlN-based wurtzite alloys have also drawn attention for direct, monolithic integration with semiconductor devices based on tetrahedrally-bonded Si and GaN. Heterostructural AlN-based alloys (Figure 1a) are particularly interesting because they exhibit unique thermodynamics of mixing (Figure 1b), and electromechanical and optical properties. Alloying AlN with ScN has been found to significantly enhance the piezoelectric response, with up to 40% increase in d_{33} compared to pristine AlN.[11,12] Er^{3+} and Yb^{3+}, which are larger cations than Sc^{3+}, have been effectively substituted at $x = 0.015$ and up to approximately $x = 0.15$, respectively.[13,14] The utilization of trace amounts of Gd^{3+} ions in AlN and GaN has been primarily explored in the context of optoelectronics such as cathodoluminescence and field-emission devices.[15–17] In our recent work, we have successfully grown thin-film wurtzite Al$_{1-x}$Gd$_x$N with higher Gd content (up to $x = 0.25$)[18] than previously reported.[19–23]

While laboratory X-ray probes suggest high crystalline fidelity, it is also well known that AlN-based alloys harbor atomic-scale point defects (e.g., nitrogen vacancies) and impurities (e.g., incorporated oxygen) that strongly influence their functional properties, even when present in sub-percent levels. For example, defect-mediated non-radiative recombination (Figure 1e) reduces the external quantum efficiency (EQE) of optoelectronic devices.[24,25] Therefore, the investigation of native defects and unintentional impurities is crucial for developing defect control strategies with the ultimate goal of optimizing alloy functional properties.[26]

However, systematic interrogation of such point defects and impurities is complicated by their low concentrations relative to atomic sites, requiring sophisticated metrology (e.g., deep level transient spectroscopy, time-resolved photoluminescence, electron paramagnetic resonance) to derive indirect evidence. As such, first-principles calculations have been widely employed to predict the defect properties of materials for photovoltaics, thermoelectrics, solid-state batteries, heterogeneous catalysis etc.[27,28] Predictive modeling of point defects in alloys is particularly challenging because of the underlying site disorder. Some recent efforts focused on defect modeling in alloys and disordered phases have utilized motif-based model Hamiltonians,[29] low-Madelung energy ordered structures, or low-energy ordering combined with statistical thermodynamics.[28] We have previously developed a methodology for prediction of defect formation energy in alloys[26] by modeling with special quasirandom structures (SQS)[30] and adapting the standard defect calculation approach for disordered phases.[31]

Motivated by the growing interest in wurtzite AlN-based alloys with group-3 and rare-earth elements, we now focus on the heterostructural Al$_{1-x}$Gd$_x$N alloy in the wurtzite phase (Figure 1a). The goal of this study is to develop practical defect control strate-
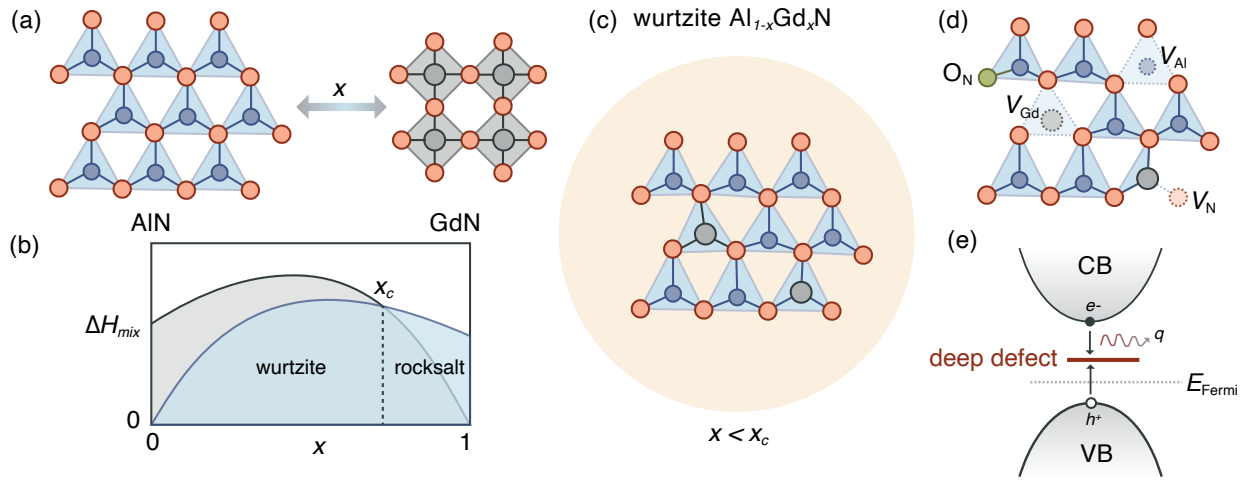
Fig. 1 (a) $Al_{1-x}Gd_xN$ are heterostructural pseudo-binary alloys between wurtzite AlN and rocksalt GdN. (b) Schematic alloy mixing enthalpy (ΔH_{mix}) curves showing wurtzite ground-state structure at Gd atomic fractions $x < x_c$. (c) Structure of wurtzite $Al_{1-x}Gd_xN$ alloy showing local distortions. (d) Native vacancies (V_{Al}, V_{Gd}, V_N) and O impurities (O_N). (e) Deep defects introduce mid-gap states that cause non-radiative carrier recombination.

gies for $Al_{1-x}Gd_xN$ alloys. Specifically, we want to answer the following questions: (1) How could we tune the synthesis conditions to reduce deleterious deep defects that cause non-radiative carrier recombination (Figure 1e)? (2) Do $Al_{1-x}Gd_xN$ alloys suffer from unintentional oxygen incorporation, common in many nitrides and nitride-based alloys?, and (3) If yes, does O incorporation exacerbate defect-mediated carrier recombination?

We use density functional theory (DFT) calculations in conjunction with our methodology for modeling defects in alloys [26] to answer these specific questions. Our calculations reveal that the dominant native deep defects in $Al_{1-x}Gd_xN$ alloys are nitrogen vacancies (V_N), which can be minimized through growth under N-rich conditions. We experimentally validate this theoretical prediction by growing $Al_{1-x}Gd_xN$ alloys as thin films while varying the nitrogen plasma power and showing a systematic suppression of sub-band gap optical absorption associated with deep defects. We also predict high levels of O incorporation on N sites in these alloys. While substitutional O_N defects do not introduce deep defect states themselves, O incorporation indirectly increases the concentration of other native deep defects by affecting the Fermi energy. Guided by our theoretical predictions, we offer practical defect control strategies that are broadly applicable to the large and growing family of wurtzite AlN-based alloys.

2 Background

The formation energy of point defects ($\Delta E_{D,q}$) is calculated using the supercell approach (see Section 5 for details). The results of the defect calculations are typically presented in the form of defect diagrams and energy level diagrams. These diagrams are useful for qualitative assessment of defect and impurity properties as well as quantitative determination of defect and electronic charge carrier (electrons, holes) concentrations.

In a defect diagram (Figure 2a), $\Delta E_{D,q}$ is plotted against the Fermi energy (E_F), which is typically referenced to the valence band maximum (VBM). For semiconductors and insulators, E_F

ranges from the VBM ($E_F = 0$) to the conduction band minimum ($E_F = E_g$, where E_g is the band gap). For degenerate semiconductors, E_F should lie inside the corresponding bands. Each set of connected lines (solid red, solid blue, dotted blue) in Figure 2a represents a defect D, which could be Al vacancy (V_{Al}), Gd vacancy (V_{Gd}), nitrogen vacancy (V_N), or substitutional O on N site (O_N) – all shown schematically in Figure 1d. The slope of the line is the charge state q. Conventionally, only the charge state q with the lowest formation energy at a given E_F is plotted.

Charged defects create electronic charge carriers – electrons and holes. A neutral defect (e.g., isoelectronic doping, alloying) does not create electronic carriers. A positively-charged defect has a positive slope in a defect diagram and represents a donor-like defect (Figure 2a). In other words, the defect ionizes to a positively-charged state by donating electron(s). Donors tend to dope the material n-type. Similarly, negatively-charged defects are acceptor-like and tend to dope p-type.

The charge transition level (q/q') of a defect is the Fermi energy at which the formation energies of charge states q and q' are equal. On a defect diagram, charge transition levels (CTLs) are identified by points at which the slope of the defect lines changes. A defect can have multiple CTLs, or they can be absent within the band gap. In Figure 2a, defects D1 and D3 have one CTL, while defect D2 has no CTL. The CTLs represent the approximate energetic location of defect states (also, defect levels) inside the band gap. These defect states can be *shallow* or *deep* depending on their carrier trapping nature.

The energetic location of a CTL relative to a band edge is essentially the thermal energy needed to ionize the defect i.e., release the electronic carrier for conduction. For a donor defect, the CTL relative to the conduction band edge is relevant. Similarly, for an acceptor defect, the CTL location from the valence band edge is relevant. How far the CTL is from the relevant band edge determines if a defect is "shallow" or "deep" (and how deep). When a defect has no CTLs inside the band gap (D2 in Figure 2a), it
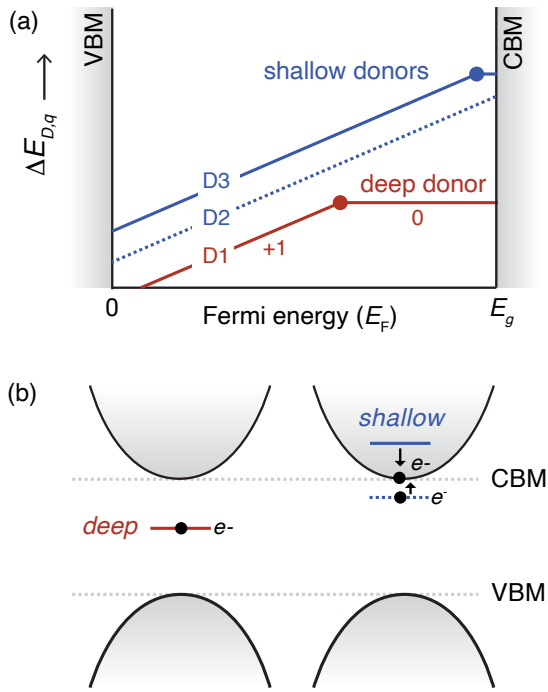
Fig. 2 (a) A schematic defect diagram showing defect formation energy ($\Delta E_{D,q}$) plotted against the Fermi energy (E_F). (b) Deep defects introduce mid-gap states far from the relevant band edges while shallow defect states are close to the band edges or resonant states inside the bands.

implies that the defect state(s) lies inside the bands. Such defects are "shallow" defects, which are considered benign for optoelectronics. Another case of a shallow defect is when the CTL is close to the corresponding band edge (donor CTL relative to CBM, acceptor CTL relative to VBM), typically within a few k_BT, where k_B is the Boltzmann constant. For example, D3 is a shallow defect. By extension, it should be clear that "deep" defects have CTLs far from the corresponding band edges, typically more than few k_BT (e.g., D1). Electronic carriers are trapped at these defect sites; such carriers cannot contribute to the electrical conductivity, unlike free carriers (Figure 2b). Deep defects states also act as centers for non-radiative carrier recombination. The CTLs are often graphically summarized as *energy level diagrams*, with each CTL labelled with the corresponding q/q' (Figure 3g).

$\Delta E_{D,q}$ depends on the elemental chemical potentials μ_i (see Section 5), which intimately depend on the chemical environment prevalent during synthesis. Forming defects involves exchanging atoms between the material and external elemental reservoirs. This exchange requires a specific amount of energy, which is determined by the chemical potentials of the elemental reservoirs (μ_i). Here, the chemical conditions during growth dictate μ_i. For example, formation of V_N in AlN is more favorable when grown under N-poor conditions (more negative μ_i) compared to N-rich conditions (more positive μ_i).

3 Results and Discussion

We model wurtzite $Al_{1-x}Gd_xN$ alloys with special quasirandom structures (see Section 5) at different Gd contents (x = 0.042, 0.125, 0.250) where the alloy exists in the wurtzite phase. The

alloy will adopt a wurtzite ground-state structure below the critical composition x_c (Figure 1b), which was theoretically predicted to be 0.82 in our previous study.[18] We calculate the formation energetics of point defects in these alloys using a methodology based on the standard defect calculation approach adapted for alloys.[26] In addition to native defects, we also probe the extent of unintentional O incorporation in these alloys via substitution on the N site. From our theoretical predictions, we identify synthetic routes for controlling deep defects in $Al_{1-x}Gd_xN$ alloys and systematically demonstrate such control in experiments through nitrogen plasma-assisted thin-film growth and optical absorption measurements. Through this joint theory-experiment effort, we answer the following specific questions pertaining to defect control strategies in $Al_{1-x}Gd_xN$ and related AlN-based alloys.

3.1 How to tune growth conditions to reduce deep defects?

To answer this question, we systematically calculate the *effective* formation energy of point defects V_{Al}, V_{Gd}, and V_N in $Al_{1-x}Gd_xN$ alloys at x = 0.042, 0.125, 0.250. The formation energetics under N-rich and N-poor growth conditions for each x are shown in the form of defect diagrams in Figures 3(a)–(f). The equilibrium Fermi energy, $E_{F,eq}$, denoted by the vertical dotted lines, are determined self-consistently to satisfy charge neutrality at T = 1000 K, which was chosen as a representative effective temperature for thin-film growth $Al_{1-x}Gd_xN$ alloys. The defect formation energies at $E_{F,eq}$ determine the defect and associated electronic charge carrier concentrations. The band gap, calculated with the GW method (see 5), decreases with increasing x (Figure 3g), which is the expected trend considering $Al_{1-x}Gd_xN$ is an alloy between an ultra-wide band gap insulator (AlN) and a semimetal/small band gap semiconductor (GdN).[32,33]

We observe some general trends regardless of x or growth conditions (N-rich vs. N-poor). The defects are amphoteric in nature i.e., they act as donors and acceptors depending on the position of E_F. However, at $E_{F,eq}$, we find that V_{Al} and V_{Gd} act as acceptors while V_N behaves as a donor, consistent with their general defect behavior. V_N is one of the dominant defects (high concentration), especially under N-poor growth conditions. Cation vacancies (V_{Al}, V_{Gd}) and anion vacancies (V_N) introduce multiple mid-gap deep defect states (Figure 3g), which is commonly observed in many wide bandgap materials. In fact, shallow defects are completely absent in wurtzite $Al_{1-x}Gd_xN$ alloys. Deep defects introduce carrier recombination centers that are undesired in minority-carrier device applications such as light-emitting diodes. AlN and AlN-based alloys are also considered for power electronics (e.g., $Al_{1-x}Ga_xN$) and as dielectrics (e.g., $Al_{1-x}Sc_xN$) for resonators. The mid-gap deep defect states trigger premature dielectric breakdown at lower electric fields[34,35] and therefore must be eliminated or at least minimized.

The concentration of a defect D in thermodynamic equilibrium is given by: $[D_q] = N_s\, exp\left(-\Delta E_{D,q}/k_B T\right)$, where N_s is the concentration of sites where the defect can form. Since $\Delta E_{D,q}$ of defects in $Al_{1-x}Gd_xN$ depends on the elemental chemical potentials (μ_i, i = Al, Gd, N), changing the growth conditions in a way that affects μ_i is a route to tuning the concentration of deep defects, partic-
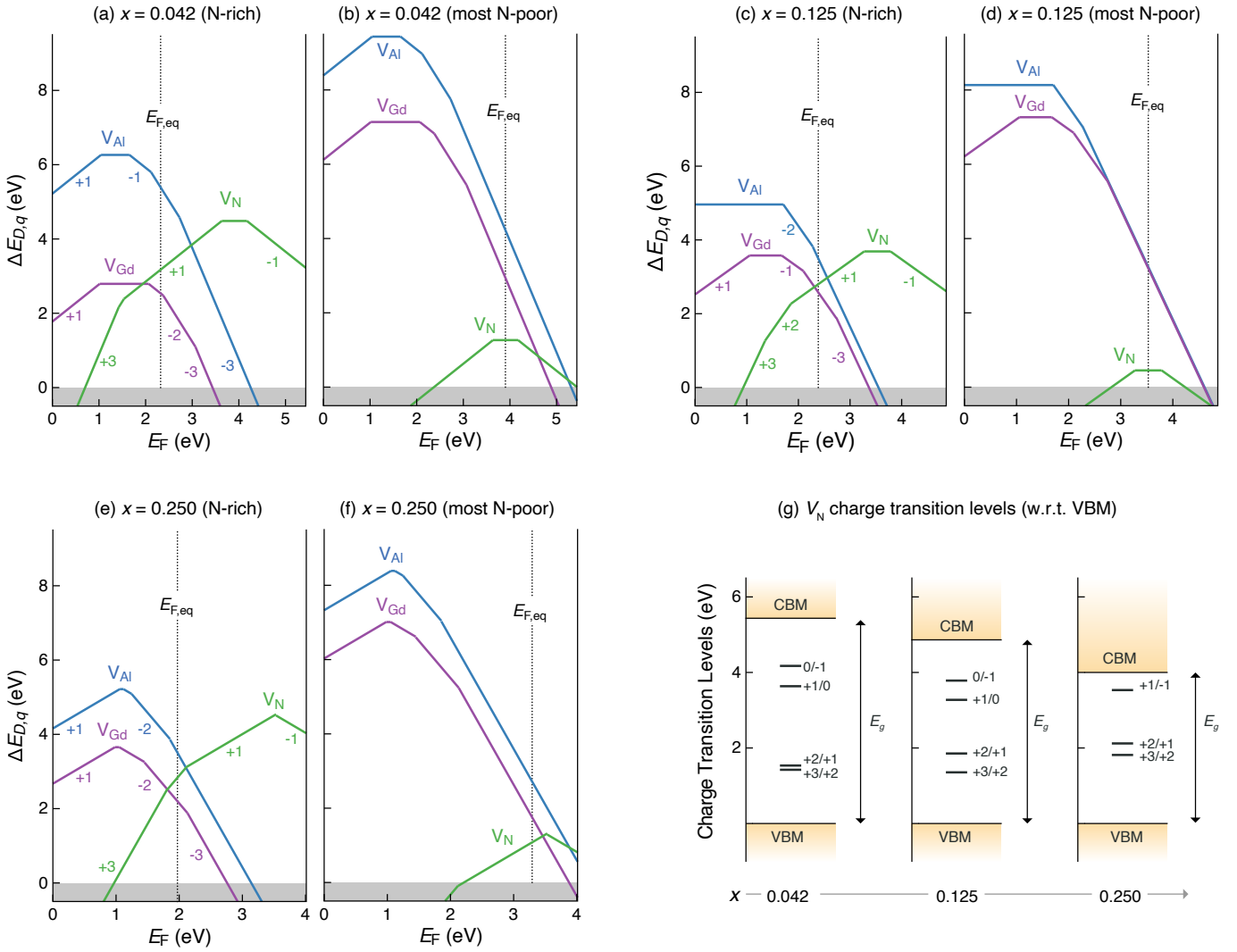
Fig. 3 Calculated defect formation energy ($\Delta E_{D,q}$) as a function of the Fermi energy (E_F) in $Al_{1-x}Gd_xN$ alloys under N-rich and most N-poor growth conditions for (a, b) $x = 0.042$, (c, d) $x = 0.125$, and (e, f) $x = 0.250$. The equilibrium Fermi energy ($E_{F,eq}$) is calculated at $T = 1000$ K. $\Delta E_{D,q}$ under N-rich conditions is consistently larger, implying lower defect concentrations. (g) Charge transition levels in $Al_{1-x}Gd_xN$ alloys at $x = 0.042$, 0.125, and 0.250. The band gap (E_g) systematically decreases with increasing Gd fraction (x).

ularly V_N. Conveniently, V_N formation energy depends on μ_N, which can be more readily manipulated because N_2 is a gaseous species. For each x, we find that V_N formation energy increases significantly (by at least 2 eV) under N-rich growth conditions compared to N-poor. Consequently, V_N concentrations in alloys grown under N-rich conditions should be significantly lower than those grown under the most N-poor conditions.

Figure 4(a) summarizes the total concentration of all deep defects (not just V_N) at each x. We predict that N-rich growth conditions will consistently result in lower concentrations of deep defects within the range of x considered in this study. In addition to introducing mid-gap defect states, charged defects create electronic carriers (electrons, holes). We calculate the *net* carrier concentration in each case (Figure 4b) as a function of temperature at which defects form and equilibrate.. Net carrier concentration is $|n_e - n_h|$, where n_e and n_h are the electron and

hole concentrations, respectively. For $n_e > n_h$ ($n_h > n_e$), the plots are labelled e^- (h^+). It should be noted that the net carriers are not *free* carriers that are responsible for electrical conduction. Due to the presence of numerous deep defect states, the carriers will be bound to the defect sites such that electrical conductivity is low. For the most N-poor growth conditions, we predict the alloys to be *n*-type doped due to the high concentration of donor V_N, with net electron concentrations systematically increasing with x. In contrast, N-rich growth conditions always result in net carrier (hole) concentrations that are several orders of magnitude lower than under the most N-poor conditions. Low background carrier concentrations are desirable in applications where AlN-based alloys are employed as dielectric insulators (e.g., ferroelectrics, piezoelectrics) or lightly-doped semiconductors (e.g., optoelectronics). *Therefore, we predict that $Al_{1-x}Gd_xN$ growth under N-rich conditions will minimize deep defects and*
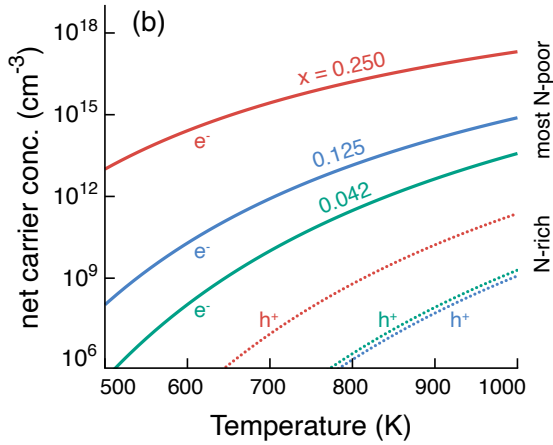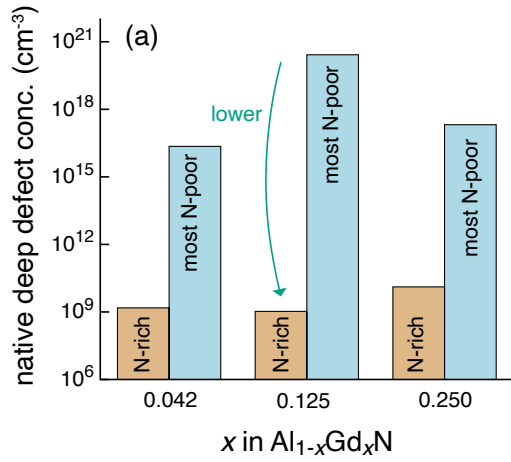
Fig. 5 Absorption coefficient α as a function of photon energy measured in thin films grown without nitrogen plasma and two different plasma powers (400 W, 600 W). Higher plasma power translates to more N-rich growth conditions, resulting in suppression of sub-band gap absorption associated with mid-gap states.

Fig. 4 (a) Total concentration of deep defects in $Al_{1-x}Gd_xN$ for $x = 0.04$, 0.125 and 0.250 under N-rich and most N-poor growth conditions. (b) Calculated net carrier concentrations as a function of temperature. The net carrier concentration is $|n_e - n_h|$, where n_e and n_h are the electron and hole concentrations, respectively. $n_e > n_h$ ($n_h > n_e$) for curves labeled e^- (h^+).

electronic carriers.

Experimental demonstration of deep defect control: To test the theoretical prediction, we synthesize thin films with a composition of $Al_{0.84}Gd_{0.16}N$ using radio-frequency (RF) magnetron co-sputtering, similar to our first work on this material.[18] We achieved N-rich conditions with a nitrogen plasma source during the deposition process (see Section 5 for details). Figure 5 illustrates the absorption spectrum of the films grown with three different nitrogen plasma conditions – no plasma, 400 W, and 600 W. The higher plasma power translates to more N-rich conditions, although direct quantification in terms of nitrogen chemical potential (μ_N) is difficult. Significant sub-band gap between $\sim$2–3 eV is attributed to the deep defect states. With increasing nitrogen plasma source power (i.e., nitrogen plasma flux), the sub-band gap absorption coefficient decreases. These results suggest that the photoabsorption around 2–3 eV originates from V_N, and the concentration of V_N decreases systematically with increasing nitrogen flux supplied during growth. The sub-band gap absorption energy around 2–3 eV is in agreement with the computed
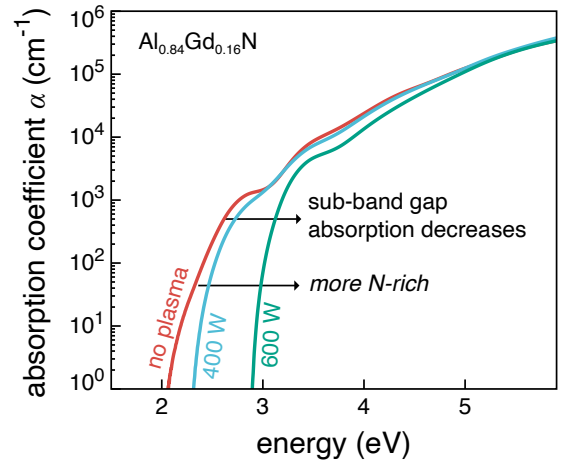
unoccupied V_N states above the $E_{F,eq}$ (Figure 3g) for $x = 0.125$, which is the alloy composition closest to the synthesized thin film ($x = 0.16$). Thus, our experimental results are consistent with the computationally predicted effects of nitrogen chemical potential (N-richness) on V_N concentration.

3.2 What is the extent of unintentional O incorporation?

Oxygen is a common impurity detected in thin films of III-N and related alloys.[36–39] Unintentional O incorporation during growth has unfavorable effects on the structural and optoelectronic properties of these materials. Oxygen substitutes on the N site, creating donor states that have been linked to temperature-activated leakage currents in AlN.[40] By extension, one expects substantial O incorporation in $Al_{1-x}Gd_xN$ alloys, but this has not been quantified. More importantly, it is not clear if O incorporation introduces additional deep defect states.

We compute the formation energy for O substitution on the N site (O_N) in $Al_{1-x}Gd_xN$ alloys at $x = 0.042$, 0.125, and 0.250. The defect diagram corresponding to $x = 0.125$ is shown in Figure 6a, while those for $x = 0.042$ and 0.250 can be found in the supplementary information (Figures S4). The general trends are consistent across different x with substitutional O_N acting as a singly-charged shallow donor defect with states $\sim$0.1 eV from the conduction band edges. This is in contrast to the native defects, which all introduce deep mid-gap states. In each case, O_N is a dominant defect under both N-rich *and* N-poor growth conditions, and therefore, *we predict high levels of O incorporation in $Al_{1-x}Gd_xN$ thin films.*

3.3 Does O incorporation exacerbate deep defects?

Substitutional O_N is a relatively shallow defect with low formation energy compared to the native defects. Naively, one would expect that the overall concentration of deep defects would remain unchanged even after O incorporation. However, the intro-
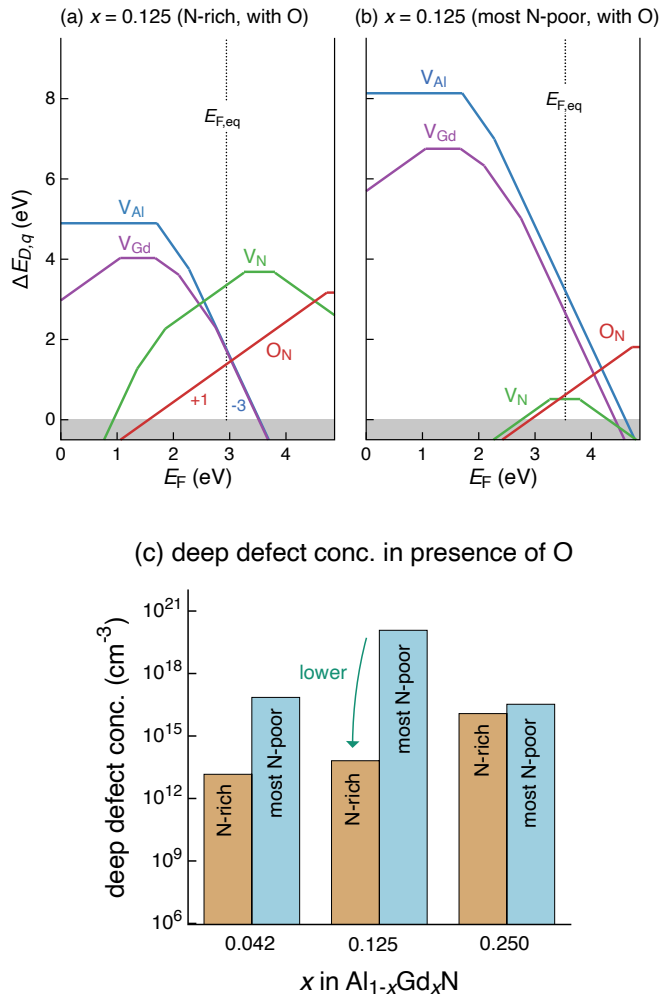
(a) $x = 0.125$ (N-rich, with O)   (b) $x = 0.125$ (most N-poor, with O)

(c) deep defect conc. in presence of O

Fig. 6 Calculated defect formation energy ($\Delta E_{D,q}$) as a function of the Fermi energy (E_F) in $Al_{0.875}Gd_{0.125}N$ alloys under N-rich and most N-poor growth conditions in the presence of oxygen. The equilibrium Fermi energy ($E_{F,eq}$) is calculated at $T = 1000$ K. O_N is a dominant defect under both N-rich and most N-poor conditions. (b) Total concentration of deep defects in $Al_{1-x}Gd_xN$ for $x = 0.04$, 0.125, and 0.250 when unintentional O incorporation is taken into account.

duction of shallow O_N has an indirect and unexpected effect on the deep defect concentrations – the low formation energy of O_N shifts the $E_{F,eq}$ and concomitantly changes the concentration of native deep defects.

Since N-rich growth conditions are desirable to suppress V_N formation (Section 3.1), Table 1 presents a comparison of the total concentration of deep defects under N-rich conditions without and with O incorporation. We find that due to the shift in $E_{F,eq}$, deep defect concentrations increase by 4-6 orders of magnitude with larger increases at higher x. However, we predict that the absolute concentrations are still relatively low (10^{16} cm^{-3} is in the ppm range) under N-rich growth conditions. The deep defect concentrations under N-poor conditions are much higher, as expected (Figure 6c).

Prior experimental efforts to reduce O incorporation in AlN and related materials have involved thin-film growth under reducing

Table 1 Total concentration of deep defects (in cm^{-3}) in different $Al_{1-x}Gd_xN$ compositions under N-rich growth conditions with and without unitentional O incorporation.

x	N-rich (without O) (cm^{-3})	N-rich (with O) (cm^{-3})
0.042	1.5×10^9	1.5×10^{13}
0.125	1.1×10^9	6.5×10^{13}
0.250	1.3×10^{10}	1.2×10^{16}

conditions e.g., by using H_2/N_2 plasma or NH_3. [36,41] Based on our calculations, *we predict that O incorporation exacerbates deep defect formation, and we recommend adopting experimental growth strategies that simultaneously achieve N-rich and reducing conditions to minimize O incorporation and V_N formation.*

4 Conclusions

Using alloy modeling and point defect calculations, we identify that V_N is one of the dominant defects in heterostructural $Al_{1-x}Gd_xN$ alloys in the wurtzite phase, especially when thin films are grown under N-poor conditions. The native vacancies (V_{Al}, V_{Gd}, V_N) are all deep defects that introduce mid-gap states – undesirable for optoelectronics as well as dielectric applications that require large electric fields. We predict and experimentally demonstrate the reduction of sub-band gap deep defects through thin-film growth in N-rich environments. We also predict significant O incorporation in $Al_{1-x}Gd_xN$ thin films, which indirectly increases the concentration of deep defects. As practical defect control strategies, we recommend growth under N-rich and reducing conditions to minimize deep defects and unintentional O incorporation in $Al_{1-x}Gd_xN$ alloys. We believe these strategies will be broadly applicable to wurtzite III-N and related alloys.

5 Methods

5.1 Alloy Modeling

$Al_{1-x}Gd_xN$ alloys were modeled with special quasirandom structures (SQS). [30] The construction of an SQS involves a stochastic search over possible configurations of local environments in a supercell to best reproduce the pairwise correlation of a fully random alloy. An optimal SQS minimizes the root-mean-square deviation from the random pairwise correlation. The SQS supercells were constructed using the Alloy Theoretic Automated Toolkit (ATAT). [42] We created 48-atom SQS supercells to model the wurtzite-phase alloys. In constructing the SQS, we considered a range of up to 4.5 Å and 3.2 Å for pair and triplet clusters, respectively. The SQS supercells were relaxed (volumes, cell geometry, and atomic positions) with DFT until the residual forces on each atom were below 0.01 eV/Å. DFT calculations were performed with plane-wave basis Vienna Ab-initio Simulation Package (VASP), [43] using the generalized gradient approximation (GGA) of Perdew-Burke-Ernzerhof (PBE) as the exchange correlation functional. [44] The following projector-
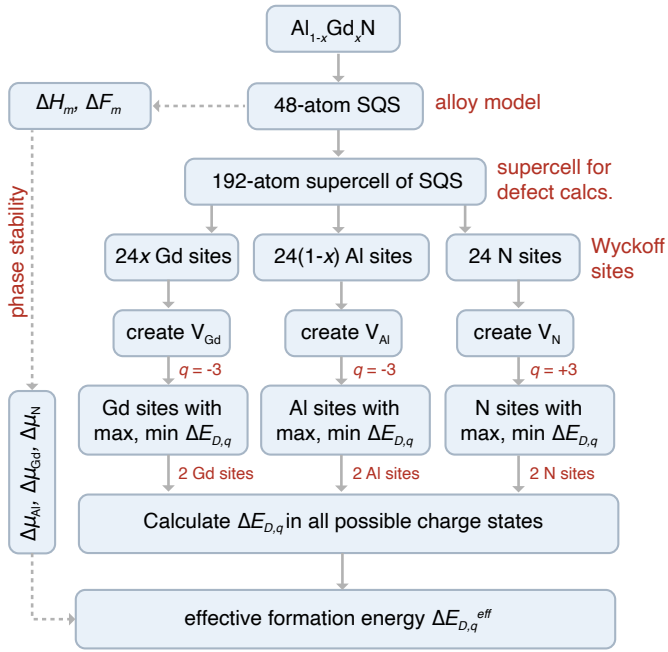
Fig. 7 Computational workflow to calculate the effective formation energy of point defects in $Al_{1-x}Gd_xN$ alloys.

augmented wave (PAW) potentials[45] were used to treat the core electons: Al 04Jan2001, N_s 07Sep2000, Gd_3 06Sep2000, and O_s 07Sep2000. The Gd_3 pseudopotential has the $4f$ electrons frozen in the core. In our previous study, we extensively tested the suitability of using the Gd_3 pseudopotential.[18]

We considered 12 different compositions (x) to calculate the alloy mixing enthalpy (ΔH_m) in the wurtzite phase, shown in Figure S1. ΔH_m is calculated as:

$$\Delta H_m = H_{alloy} - xH_{GdN} - (1-x)H_{AlN} \qquad (1)$$

where H_{alloy} is the enthalpy of the alloy, and H_{GdN} and H_{AlN} are the enthalpy of rocksalt GdN and wurtzite AlN, respectively. The mixing free energy was then calculated using, $\Delta F_m = \Delta H_m - T\Delta S_m$. Here, only the configurational entropy contribution to ΔS_m was considered and is given by:

$$\Delta S_m = -k_B \left[xln(x) + (1-x)ln(1-x) \right] \qquad (2)$$

The vibrational contributions to ΔS_m are typically neglected as they are small compared to the configurational contribution, especially at higher temperatures. We used the calculated ΔF_m to compute the grand potential phase diagrams and establish the ranges of elemental chemical potentials that satisfy phase stability of the alloys. See Section 5.3 for details.

5.2 Defect Calculations

We adapted the standard supercell approach to calculate the defect formation energetics in $Al_{1-x}Gd_xN$ alloys. We have previously used this approach to model defects in $Ba_{2(1-x)}Sr_{2x}CdP_2$ Zintl phase alloys.[26] The computational workflow is schematically illustrated in Figure 7. Starting from the 48-atom SQS described in

the previous section, we constructed 192-atom supercells for performing defect calculations. Here, the SQS is treated as a "unit cell" of the alloy. Since the SQS has $P1$ symmetry i.e., each atom has only one symmetry-equivalent position, there are 48 Wyckoff sites in the 192-atom supercells. For each Wyckoff site of Gd, Al, and N, we created supercells with vacancies and calculated the defect formation energy ($\Delta E_{D,q}$) in a single charge state q (V_{Gd}^{-3}, V_{Al}^{-3}, V_N^{+3}) that is most favorable based on a simple ionic picture. We then identified the Wyckoff sites associated with the maximum and minimum $\Delta E_{D,q}$ for each type of vacancy defect (Figure S5 for $x = 0.125$). For these identified sites (2 each for Gd, Al, and N), we performed a more comprehensive set of defect calculations by considering all plausible charge states. By considering the sites with maximum and minimum $\Delta E_{D,q}$, it allows us to build statistics of $\Delta E_{D,q}$ and compute effective formation energies $\Delta E_{D,q}^{eff}$, which capture the effect of different local environments in an alloy.

$\Delta E_{D,q}$ of defect D in charge state q was calculated using the periodic supercell approach and is given by the equation,

$$\Delta E_{D,q} = E_{D,q} - E_{host} + \sum_i n_i \mu_i + qE_F + E_{corr} \qquad (3)$$

where $E_{D,q}$ and E_{host} are the total energies of the supercell with and without the defect, respectively. E_F is the Fermi energy, which is referenced to the valence band maximum. n_i is the number of atoms of element i added ($n_i < 0$) or removed ($n_i > 0$) to create the defect D. E_{corr} term contains the finite-size corrections, which are calculated following the methodology of Lany and Zunger.[46] The finite-size corrections include: (1) image charge correction for charged defects, (2) potential alignment correction for charged defects, and (3) band-filling correction for shallow defects. The open-source Python package, pylada-defects, was employed to generate defect supercells and calculate the finite-size corrections.[47]

The underestimation of the band gap in DFT was corrected by applying individual valence and conduction band edge shifts (relative to the DFT-computed band edges) as determined from GW quasiparticle energies.[46,48] We used DFT wave functions as initial wavefunctions for the GW calculations. The GW eigen-energies were iterated to self-consistency, removing the dependence on the single-particle energies of the initial DFT calculations. The DFT wave functions were kept constant during the GW calculations, which allows the interpretation of the GW eigen-energies in terms of energy shifts relative to the Kohn-Sham energies. The GW quasi-particle energies were calculated for the 48-atom SQS for each x using a $2 \times 2 \times 2$ k-point grid, which correctly captures the k-point position of the band edges as verified against DFT calculations performed on dense k-point grids.

In our defect calculations, we considered cation (Al, Gd) and anion (N) vacancies, but did not include cation antisites i.e., Al_{Gd}, Gd_{Al}, because these isoelectronic antisites are already accounted for through site disorder. We also did not consider interstitials because they are found to have high formation energies in AlN and related materials.[49]

5.3 Chemical Potentials and Phase Stability

Elemental chemical potentials μ_i (i = Al, Gd, N, O) in Eq. 3 are expressed relative to the reference state chemical potentials (μ_i^0) such that $\mu_i = \mu_i^0 + \Delta\mu_i$, where $\Delta\mu_i$ is the deviation from the reference state. μ^0 are fitted to a set of measured formation enthalpy of compounds (standard conditions) in the quaternary Al-Gd-N-O chemical space. Specifically, μ^0 for Gd is obtained by fitting to experimental formation enthalpy of Gd_2O_3 and μ_O^0 = -4.80 eV.[50] Table S1 lists the fitted μ^0 for Al, Gd, N, and O.

For a material, the accessible range of $\Delta\mu_i$ is constrained by the condition of its thermodynamic phase stability and is calculated by constructing the convex hull in the grand potential phase diagram. At each x, we treated $Al_{1-x}Gd_xN$ alloy as a line compound that lies on the convex hull. The mixing free energy ΔF_m (Section 5.1) was used to compute the convex hull and obtain the range of $\Delta\mu_i$ for which the alloy is stable. Tables S2–S4 lists the calculated $\Delta\mu_i$ values for different x at the vertices of the convex hull that define the region of phase stability in the ternary Al-Gd-N chemical space. Figure S2 shows the corresponding phase diagram in the composition space for x = 0.25. The vertices V1–V4 labelled in Figure S2 correspond to the vertices in Table S4. Similarly, Tables S5–S7 lists the calculated $\Delta\mu_i$ values in the quaternary Al-Gd-N-O chemical space.

Unlike solids, the chemical potential of gaseous elements strongly depend on their partial pressures and processing temperatures. For example, higher O_2 partial pressures and lower temperatures give rise to more O-rich conditions. In this work, we utilized the rigid-dumbbell ideal gas model[51] to calculate the O chemical potential $\mu_O(T, p_{O_2})$ at T = 1000 K and p_{O_2} = 0.2 atm,

$$\mu_O(p_{O_2}, T) = \mu_O^0 + \Delta\mu_O(T) + \frac{1}{2}k_B T \ln(p_{O_2}) \quad (4)$$

where μ_O^0 is the oxygen reference chemical potential at standard conditions and $\Delta\mu_O(T)$ is defined by the rigid dumbbel model as,

$$\begin{aligned}\Delta\mu_O(T) &= \frac{1}{2}\left(\Delta H_{O_2}(T) - T\Delta S_{O_2}(T)\right) \\ &= \frac{1}{2}C_P^0\left(T - T^0\right) - \frac{1}{2}T\left(S_{O_2}^0 + C_P^0\ln\left(\frac{T}{T^0}\right)\right)\end{aligned} \quad (5)$$

where $C_P^0 = 7k_B/2$ = 0.000302 eV/K, $S_{O_2}^0$ = 0.0021 eV/K,[52] T^0 = 298.15 K. Since the fitted reference chemical potential represents the standard state, the term of $H_{O_2}^0$, which was originally included in Ref. 51 is already included in the fitted reference chemical potential and thus, not included in Eqn. 5. However, we did not explicitly consider the temperature dependency of N chemical potential since our experimental setup employed non-equilibrium methods for thin-film growth, including the use of nitrogen plasma, which can achieve more N-rich conditions than set by the thermodynamic limit. To approximately capture the N-rich condition of the non-equilibrium growth within the thermodynamic framework, we used the nitrogen reference chemical potential, which is higher than the high-temperature equilibrium thermodynamic limit.

5.4 Defect and Carrier Concentrations

We generalized the formalism of computing defect formation energy by defining an effective formation energy $\Delta E_{D,q}^{eff}$.[53] Mathematically, we calculated $\Delta E_{D,q}^{eff}$ from the sites with maximum and minimum $\Delta E_{D,q}$,

$$exp\left(-\frac{\Delta E_{D,q}^{eff}}{k_B T}\right) = 0.5\left[exp\left(-\frac{\Delta E_{D,q}^{min}}{k_B T}\right) + exp\left(-\frac{\Delta E_{D,q}^{max}}{k_B T}\right)\right] \quad (6)$$

where $\Delta E_{D,q}^{min}$ and $\Delta E_{D,q}^{max}$ correspond to sites with minimum and maximum defect formation energy (Figure 7), k_B is the Boltzmann constant, and T is temperature. We calculated the $E_{F,eq}$ and corresponding defect and charge carrier concentrations by self-consistently solving for overall charge neutrality. We used py-scp-fermi to calculate the self-consistent $E_{F,eq}$.[54,55]

5.5 Thin-film Growth and Characterization

$Al_{0.84}Gd_{0.16}N$ thin films were deposited with reactive radio-frequency (RF) co-sputtering from elemental targets in a vacuum chamber with base pressure of 10^{-7} Torr. The substrates were held at 400 °C during growth, at which the chamber partial pressures are p_{O_2} < 2×10^{-8} Torr and p_{H_2O} < 1×10^{-8} Torr. The powers used were 150 W (Al, 99.999%) and 40 W (Gd, 99.5%) for the 2" targets. Deposition occurred at a total chamber pressure of 2 mTorr under 5 sccm of Ar and 15 sccm of N_2 (99.999%) gases, where the nitrogen was introduced through an inductively coupled plasma source. The power of the nitrogen plasma source was varied (0 W, 400 W, 600 W) to create different nitrogen plasma flux conditions. A cryogenic sheath was employed to trap adventitious oxygen or water during deposition. The targets were pre-sputtered for 20 min with the substrate shutter closed, followed by a 70 min deposition with an approximate deposition rate of 3.5 nm/min. Films were grown on (100) p-Si substrate with native oxide at the surface; no substrate pretreatment was performed. Cation composition was measured with X-ray fluorescence (XRF) using a Bruker M4 Tornado under vacuum (~15 Torr).

Spectroscopic ellipsometry data were acquired at 75° incident angle on homogeneous films grown with different nitrogen plasma source conditions (0 W, 400 W, and 600 W) on crystalline pSi(100) substrates using a J.A. Woollam Co. RC2-XI ellipsometer. CompleteEASE software (version 5.13) was used to model the data by fitting the real and imaginary parts of the dielectric function with a four-layer model consisting of the silicon substrate, native silicon oxide, the $Al_{1-x}Gd_xN$ film, and surface roughness approximated with a standard mixed film/void Bruggeman EMA layer. The silicon and native oxide were modeled using well-known optical constants provided by the CompleteEASE software. The $Al_{1-x}Gd_xN$ films were modeled using a generic absorbing film on silicon utilizing b-spline parameterization.

Acknowledgements

Conflicts of Interest

There are no conflicts of interest to declare.

References

1 F. Ponce and D. Bour, *Nature*, 1997, **386**, 351–359.

2 N. Sinha, G. E. Wabiszewski, R. Mahameed, V. V. Felmetsger, S. M. Tanner, R. W. Carpick and G. Piazza, *Applied Physics Letters*, 2009, **95**, 053106.

3 M. Akiyama, T. Kamohara, K. Kano, A. Teshigahara, Y. Takeuchi and N. Kawahara, *Advanced Materials*, 2009, **21**, 593–596.

4 Y. Taniyasu, M. Kasu and T. Makimoto, *nature*, 2006, **441**, 325–328.

5 S. Fichtner, N. Wolff, F. Lofink, L. Kienle and B. Wagner, *J. Appl. Phys.*, 2019, **125**, 114103.

6 Y. Kusano, G.-L. Luo, D. Horsley, I. Taru Ishii and A. Teshigahara, 2018 IEEE International Ultrasonics Symposium (IUS), 2018, pp. 1–4.

7 T. Yokoyama, Y. Iwazaki, Y. Onda, T. Nishihara, Y. Sasajima and M. Ueda, *IEEE transactions on ultrasonics, ferroelectrics, and frequency control*, 2015, **62**, 1007–1015.

8 K. Yazawa, J. S. Mangum, P. Gorai, G. L. Brennecka and A. Zakutayev, *Journal of Materials Chemistry C*, 2022, **10**, 17557–17566.

9 K. R. Talley, S. L. Millican, J. Mangum, S. Siol, C. B. Musgrave, B. Gorman, A. M. Holder, A. Zakutayev and G. L. Brennecka, *Physical Review Materials*, 2018, **2**, 063802.

10 K. Yazawa, D. Drury, A. Zakutayev and G. L. Brennecka, *Applied Physics Letters*, 2021, **118**, 162903.

11 O. Zywitzki, T. Modes, S. Barth, H. Bartzsch and P. Frach, *Surface and Coatings Technology*, 2017, **309**, 417–422.

12 P. Daoust, P. Desjardins, R. Masut, V. Gosselin and M. Côté, *Physical Review Materials*, 2017, **1**, 055402.

13 A. Kabulski, V. Pagán and D. Korakakis, *MRS Online Proceedings Library (OPL)*, 2008, **1129**, 1129–V09.

14 T. Yanagitani and M. Suzuki, *Applied Physics Letters*, 2014, **104**, 082911.

15 N. Teraguchi, A. Suzuki and Y. Nanishi, Materials Science Forum, 2002, pp. 1477–1480.

16 J. B. Gruber, U. Vetter, H. Hofsäss, B. Zandi and M. F. Reid, *Physical Review B*, 2004, **69**, 195202.

17 T. Kita, S. Kitayama, M. Kawamura, O. Wada, Y. Chigi, Y. Kasai, T. Nishimoto, H. Tanaka and M. Kobayashi, *Applied Physics Letters*, 2008, **93**, 211901.

18 R. W. Smaha, K. Yazawa, A. G. Norman, J. S. Mangum, H. Guthrey, G. L. Brennecka, A. Zakutayev, S. R. Bauers, P. Gorai and N. M. Haegel, *Chemistry of Materials*, 2022, **34**, 10639–10650.

19 N. Teraguchi, A. Suzuki and Y. Nanishi, *Materials Science Forum*, 2002, **389-393**, 1477–1480.

20 T. Kita, S. Kitayama, M. Kawamura, O. Wada, Y. Chigi, Y. Kasai, T. Nishimoto, H. Tanaka and M. Kobayashi, *Applied Physics Letters*, 2008, **93**, 211901.

21 Y. Chen, X. Shi, J. Yang and Y. Chen, *Physica Status Solidi (C)*, 2012, **9**, 1040–1042.

22 S. W. Choi, Y. K. Zhou, S. Emura, X. J. Lee, N. Teraguch, A. Suzuki and H. Asahi, *Physica Status Solidi (C)*, 2006, **3**, 2250–2253.

23 K. Fukui, S. Sawai, T. Ito, S. Emura, T. Araki and A. Suzuki, *Physica Status Solidi (C)*, 2010, **7**, 1878–1880.

24 D. Luo, R. Su, W. Zhang, Q. Gong and R. Zhu, *Nature Rev. Mater.*, 2020, **5**, 44–60.

25 R. E. Brandt, J. R. Poindexter, P. Gorai, R. C. Kurchin, R. L. Hoye, L. Nienhaus, M. W. Wilson, J. A. Polizzotti, R. Sereika, R. Zaltauskas *et al.*, *Chem. Mater.*, 2017, **29**, 4667–4674.

26 J. Qu, A. Balvanz, S. Baranets, S. Bobev and P. Gorai, *Materials Horizons*, 2022, **9**, 720–730.

27 P. Gorai, D. Krasikov, S. Grover, G. Xiong, W. K. Metzger and V. Stevanović, *Science Advances*, 2023, **9**, eade3761.

28 P. Gorai, H. Long, E. Jones, S. Santhanagopalan and V. Stevanović, *Journal of Materials Chemistry A*, 2020, **8**, 3851–3858.

29 J. Pan, J. Cordell, G. J. Tucker, A. C. Tamboli, A. Zakutayev and S. Lany, *Advanced Materials*, 2019, **31**, 1807406.

30 A. Zunger, S.-H. Wei, L. Ferreira and J. E. Bernard, *Physical review letters*, 1990, **65**, 353.

31 S. Lany and A. Zunger, *Physical Review B*, 2008, **78**, 235104.

32 P. Wachter, *Advances in Materials Physics and Chemistry*, 2016, **06**, 28–46.

33 H. Yoshitomi, S. Kitayama, T. Kita, O. Wada, M. Fujisawa, H. Ohta and T. Sakurai, *Physical Review B*, 2011, **83**, 155202.

34 P. Gorai, R. W. McKinney, N. M. Haegel, A. Zakutayev and V. Stevanovic, *Energy & Environmental Science*, 2019, **12**, 3338–3347.

35 Y. Sun, S. A. Boggs and R. Ramprasad, *Applied Physics Letters*, 2012, **101**, 132906.

36 N. Gungor and M. Alevli, *Journal of Vacuum Science & Technology A: Vacuum, Surfaces, and Films*, 2022, **40**, 022404.

37 J. Casamento, H. G. Xing and D. Jena, *physica status solidi (b)*, 2020, **257**, 1900612.

38 M. Moram, Z. Barber and C. Humphreys, *Thin Solid Films*, 2008, **516**, 8569–8572.

39 J. L. Lyons and C. G. Van de Walle, *NPJ Computational Materials*, 2017, **3**, 12.

40 M. Schneider, A. Bittner and U. Schmid, *Sensors and Actuators A: Physical*, 2015, **224**, 177–184.

41 L. Tian, S. Ponton, M. Benz, A. Crisci, R. Reboud, G. Giusti, F. Volpi, L. Rapenne, C. Vallée, M. Pons *et al.*, *Surface and Coatings Technology*, 2018, **347**, 181–190.

42 A. Van De Walle, *Calphad*, 2009, **33**, 266–278.

43 G. Kresse and J. Furthmüller, *Physical review B*, 1996, **54**, 11169.

44 J. P. Perdew, K. Burke and M. Ernzerhof, *Physical review letters*, 1996, **77**, 3865.

45 P. E. Blöchl, *Physical review B*, 1994, **50**, 17953.

46 S. Lany and A. Zunger, *Physical Review B*, 2008, **78**, 235104.

47 A. Goyal, P. Gorai, H. Peng, S. Lany and V. Stevanović, *Computational Materials Science*, 2017, **130**, 1–9.

48 H. Peng, D. O. Scanlon, V. Stevanovic, J. Vidal, G. W. Watson and S. Lany, *Physical Review B*, 2013, **88**, 115201.

49 A. Szállás, K. Szász, X. T. Trinh, N. T. Son, E. Janzén and A. Gali, *Journal of Applied Physics*, 2014, **116**, 113702.

50 V. Stevanović, S. Lany, X. Zhang and A. Zunger, *Physical Review B*, 2012, **85**, 115104.

51 J. Osorio-Guillén, S. Lany, S. V. Barabash and A. Zunger, *Phys. Rev. Lett.*, 2006, **96**, 107203.

52 W. Haynes, *CRC Handbook of Chemistry and Physics*, CRC Press, 2014.

53 X. Zhang, J. Kang and S.-H. Wei, *Nature Computational Science*, 2023, **3**, 210–220.

54 J. Buckeridge, D. Jevdokimovs, C. Catlow and A. Sokol, *Physical Review B*, 2016, **94**, 180101.

55 J. Buckeridge, *Computer Physics Communications*, 2019, **244**, 329–342.